JGR Atmospheres

RESEARCH ARTICLE
10.1029/2023JD039383

Construction of a Clear-Sky Three Dimensional Sub-Grid Terrain Long-Wave Radiative Effect Parameterization Scheme Under Isotropic Assumption

Chunlei Gu[1], Anning Huang[1,2], Xin Li[3], Ben Yang[1], and Yang Wu[3]

[1]School of Atmospheric Sciences, Nanjing University, Nanjing, China, [2]Qinghai Lake Comprehensive Observation Research Station, Chinese Academy of Sciences, Gangcha, China, [3]Key Laboratory of Transportation Meteorology of China Meteorological Administration, Nanjing Joint Institute for Atmospheric Sciences, Chinese Academy of Meteorological Sciences - Jiangsu Meteorological Service, Nanjing, China

Key Points:

- A clear-sky three-dimensional sub-grid terrain long-wave radiative effect (3DSTLRE) parameterization scheme has been developed
- The 3DSTLRE scheme shows high accuracy and is portable to the models with different horizontal resolutions
- Without considering the 3DSTLRE, the surface downwelling long-wave radiation over the rugged terrain areas is underestimated

Correspondence to:
A. Huang,
anhuang@nju.edu.cn

Citation:
Gu, C., Huang, A., Li, X., Yang, B., & Wu, Y. (2024). Construction of a clear-sky three dimensional sub-grid terrain long-wave radiative effect parameterization scheme under isotropic assumption. *Journal of Geophysical Research: Atmospheres*, *129*, e2023JD039383. https://doi.org/10.1029/2023JD039383

Received 3 JUN 2023
Accepted 3 FEB 2024

Author Contributions:
Conceptualization: Anning Huang
Data curation: Chunlei Gu, Anning Huang, Yang Wu
Formal analysis: Chunlei Gu, Anning Huang, Xin Li, Ben Yang
Investigation: Chunlei Gu, Anning Huang, Xin Li, Ben Yang, Yang Wu
Methodology: Chunlei Gu, Anning Huang
Resources: Chunlei Gu
Software: Chunlei Gu, Anning Huang
Supervision: Anning Huang, Xin Li
Validation: Chunlei Gu, Anning Huang, Xin Li
Visualization: Chunlei Gu, Anning Huang, Ben Yang
Writing – original draft: Chunlei Gu, Anning Huang
Writing – review & editing: Chunlei Gu, Anning Huang, Xin Li, Ben Yang, Yang Wu

Abstract Rugged topography considerably regulates the surface downwelling long-wave radiation (SDLR) flux and further affects the surface radiation and energy balances. The three dimensional sub-grid terrain long-wave radiative effect (3DSTLRE) is absent in most current numerical models, which usually adopt plane-parallel schemes to simulate the SDLR flux. This study has developed a clear-sky 3DSTLRE parameterization scheme based on the isotropic assumption of SDLR at rugged terrains and systematically evaluated its ability over the Tibetan Plateau (TP). Results show that the 3DSTLRE scheme achieves good and stable performance regardless of the horizontal resolution, time of the year, and sub-grid terrain complexity. At different model horizontal resolutions ranging from 0.025° to 0.8°, the normalized mean absolute errors (NMAE) of the daily SDLR flux simulated by the clear-sky 3DSTLRE scheme over most of TP are less than 0.9%, and the NMAE of the daily SDLR flux produced by the clear-sky 3DSTLRE scheme regionally averaged over the grids with different sub-grid terrain complexity are less than 0.25% in different months. Neglecting the 3DSTLRE in the plane-parallel schemes may lead to clearly underestimated SDLR flux over the rugged areas, and the underestimation increases with the horizontal resolution and sub-grid terrain complexity. At different model horizontal resolutions, the mean underestimation of the clear-sky daily SDLR flux simulated by the plane-parallel scheme over most of TP ranges from 5 to 20 $W \cdot m^{-2}$ with a relative underestimation of 4∼10%. The 3DSTLRE scheme can clearly reduce the biases of plane-parallel scheme and exhibits wide application prospects in various numerical models.

Plain Language Summary Terrain greatly affects the surface downwelling long-wave radiation (SDLR) flux and further modulates the surface radiation and energy balance and thereafter weather and climate at local to regional scales. But most current numerical models do not consider the 3-dimensional sub-grid terrain long-wave radiative effect (3DSTLRE). This study has developed a clear-sky 3DSTLRE parameterization scheme to describe the 3DSTLRE in the numerical models. Several experiments have been conducted to test the accuracy of the 3DSTLRE parameterization scheme in Tibetan Plateau and to indicate the necessity of considering the 3DSTLRE over the areas with rugged sub-grid terrains in numerical models. Results show that the clear-sky 3DSTLRE scheme can accurately calculate the SDLR flux at the model grids with different horizontal resolutions. The plane-parallel schemes without considering the 3DSTLRE tend to clearly underestimate the SDLR flux over the rugged areas. The 3DSTLRE parameterization scheme can obviously reduce the biases of the SDLR flux simulated by the plane-parallel scheme over the regions with complex terrain. Due to the advantages of a solid physical foundation, high accuracy, and strong flexibility, the 3DSTLRE scheme developed in this study exhibits wide application prospects in various numerical models.

1. Introduction

Surface long-wave radiation fluxes are important components of the land surface energy budgets (Hu et al., 2017; Jiao & Mu, 2022; Matzinger et al., 2003). Surface upwelling long-wave radiation cools land, heats atmosphere, and during nighttime dominates surface energy balances (Pashiardis et al., 2017; Stephens et al., 2012). Surface downwelling long-wave radiation (SDLR) results from atmospheric greenhouse effects and responds quickly to global warming (Ma et al., 2014; Shakespeare & Roderick, 2022; Vargas Zeppetello et al., 2019). Thus, surface

long-wave radiation fundamentally affects the land surface energy processes, atmospheric circulation, and variation of climate (Laguë et al., 2019; Wild, 2020; Yu & Zhang, 2015; Zeng et al., 2017).

Over plane surface, the surface upwelling and downwelling long-wave radiation fluxes depend on the land surface temperature, land surface emissivity, and condition of low-level atmosphere, that is, temperature, humidity, cloud, aerosol, and greenhouse gasses (Ma et al., 2014; Morcrette, 2002; Panicker et al., 2008). Due to complicated influencing factors, it is tough to accurately simulate the surface long-wave radiation (Chen et al., 2017; Li et al., 2013; Wild et al., 1995). The surface long-wave radiation simulation can be improved from better model description of land surface process (Zheng et al., 2012) and cloud-aerosol radiative forcing (Chen et al., 2018; Jin et al., 2019; Ma et al., 2019; Peng et al., 2018; Zhang et al., 2014). However, uncertainties in the simulated surface long-wave radiation over rugged areas (i.e., the Tibetan Plateau (TP), Andes Mountains, and Rocky Mountains) are much larger than those over plains (Xu et al., 2021, 2022). This is attributed to the fact that the STLRE is not included in most numerical models (Feldman et al., 2022).

The topography can regulate the surface long-wave radiation (Marks & Dozier, 1979). Compared to plane surface, rugged surface receives less SDLR from the atmosphere due to terrain obstruction but gets additional long-wave radiation emitted from adjacent terrain (Gratton et al., 1993; Oliphant et al., 2003). The terrain-emitted long-wave radiation accounts for about 22% (more than 50%) of the total SDLR in the common (extreme) cases over the Upper Colorado River Basin (Feldman et al., 2022). The SDLR over the north slope of a high latitude valley in Canada is increased by 60% due to the long-wave radiation from the neighboring slopes (Sicart et al., 2006). The outgoing surface net long-wave radiation observed at the crater bottom is 28% less than that at the crater rim in Arizona's Meteor Crater (Whiteman & Hoch, 2010). According to the remote sensing observation, the SDLR within the wavelength band of 10.4 ∼ 12.5 μm emitted from the adjacent terrain is about 2.6 times higher than that emitted from the atmosphere over the glacier tongue of Qiyi Glacier in China (Wu et al., 2019).

Considering the STLRE in numerical models benefits the simulation of the surface long-wave radiation or surface long-wave radiation related processes (Arnold et al., 2006; Plüss & Ohmura, 1997). The simulated melt of Shackleton Glacier increases 30% because of the long-wave radiation emitted from the surrounding valley wall (Jiskoot & Mueller, 2012). Simulations indicate that $81 \sim 120\ W \cdot m^{-2}$ of long-wave radiation emitted from the surrounding bare rocks to the margin of the Cuchillacocha Glacier leads to 1.7 m of glacier melt during the dry season (Aubry-Wake et al., 2018). Without considering the STLRE, the biases of simulated surface net long-wave radiation reach to the magnitude of $\sim 10^2\ W \cdot m^{-2}$ (∼100%) over the highly rugged surface (Yan et al., 2016, 2020).

The importance of describing the sub-grid terrain solar radiative effect in the numerical studies of the weather/climate has been recognized since the 2000s (Hauge & Hole, 2003; Müller & Scherer, 2005; Zhang et al., 2002). The sub-grid terrain solar radiative effect is prosperously adopted in the numerical studies of weather and climate with the parameterization schemes based on various theories (Arthur et al., 2018; Fan et al., 2019; Feng & Zhang, 2007; Hao et al., 2021; Huang et al., 2022; Lee et al., 2011; Manners et al., 2012). Because of the complex terrain of TP and its important role in affecting the regional and global climate (Wu et al., 2017; Yang et al., 2020), great efforts have been paid to investigate the sub-grid terrain solar radiative effect in TP (Gu et al., 2022; Hao et al., 2021; Lee et al., 2013; Zhang et al., 2002).

The sub-grid terrains not only obstruct the solar irradiance and the atmospheric downwelling long-wave radiation, but also reflect solar radiation and emit long-wave radiation to the land surface (Dozier & Frew, 1990; Duguay, 1995). Both the terrain solar and long-wave radiative effects should be described in the numerical models. However, most numerical models totally neglect the STLRE. Zhang et al. (2006) and Gu et al. (2020) introduce the 2-dimensional STLRE to the regional climate models based on the theory of Weng et al. (1981). The 2-dimensional STLRE simplifies 3D topography as 2D infinite long slope and has the disadvantage of fragmentary physical basis. The 2-dimensional STLRE only considers the terrain obstruction but completely ignores the essential long-wave radiation emitted from adjacent terrain. It is urgent to describe the 3-dimensional STLRE (3DSTLRE) in numerical models (Feldman et al., 2022).

Here comes two questions: (a) How can the 3DSTLRE be accurately parameterized in the numerical models? (b) How large are the uncertainties of the grid scale SDLR in the models without the 3DSTLRE scheme? In this study, a clear-sky 3DSTLRE parameterization scheme has been developed and its accuracy has been evaluated at different model horizontal resolutions. The differences of simulated SDLR fluxes between the traditional plane-parallel scheme and the 3DSTLRE scheme are also discussed. The rest of the paper is arranged as follows:

Table 1
List of Symbols and Abbreviations

Symbol or abbreviation	Meaning
3DSTLRE	3 Dimensional Sub-gird Terrain Long-wave Radiation Effects
a	Subscript for the atmospheric variables
C_1	3DSTLRE correction factor 1
C_2	3DSTLRE correction factor 2
d	Subscript for the dewpoint
e	Water vapor pressure
g	Subscript for the grid scale variable
i	Subscript for the sub-grid scale variable
$L_{\downarrow}$	Clear-sky surface downwelling long-wave radiation fluxes
L_{sur}	Long-wave radiation emitted from the surrounding terrains
m	Sub-grid number in the west-east direction
n	Sub-grid number in the north-south direction
NMAE	Normalized Mean Absolute Error
p	Subscript for the variables over the plane surface
PDF	Probability Density Function
s	Subscript for the ground surface variables
SDLR	Surface Downwelling Long-wave Radiation
SKV	Sky view factor
STLRE	Sub-gird Terrain Long-wave Radiation Effects
T	Temperature
t	Subscript for the variables over the rugged surface
z	Altitude
α	Slope
β	Slope orientation
ε	Long-wave emissivity
ζ	Maximal terrain elevation angle
θ	Azimuth angle
σ	Stefan-Boltzmann constant
Δx	Sub-grid scale horizontal resolution in the west-east direction
Δy	Sub-grid scale horizontal resolution in the north-south direction

Section 2 introduces the methodology, which includes the description of the explicit calculations of SDLR over rugged surface at sub-grid scale and the 3DSTLRE parameterization scheme, respectively. Data, experimental design, and evaluation metrics are presented in Section 3. Section 4 evaluates the performance of 3DSTLRE scheme. Conclusions and discussions are shown in Section 5. The acronyms and symbols used in this study are shown in Table 1.

2. Methodology

2.1. Mountain Radiation Theory

The mountain radiation theory describes the effect of 3-dimensional topography on the SDLR fluxes (Duguay, 1995; Robledano et al., 2022). The terrain obstructs the sky and reduces the atmospheric downwelling long-wave radiation flux but emits the additional long-wave radiation flux to the target land surface (Figure 1a). The terrain-emitted long-wave radiation flux is usually greater than the atmospheric downwelling long-wave radiation flux, which makes the SDLR over the rugged terrain areas larger than that over the plane surface

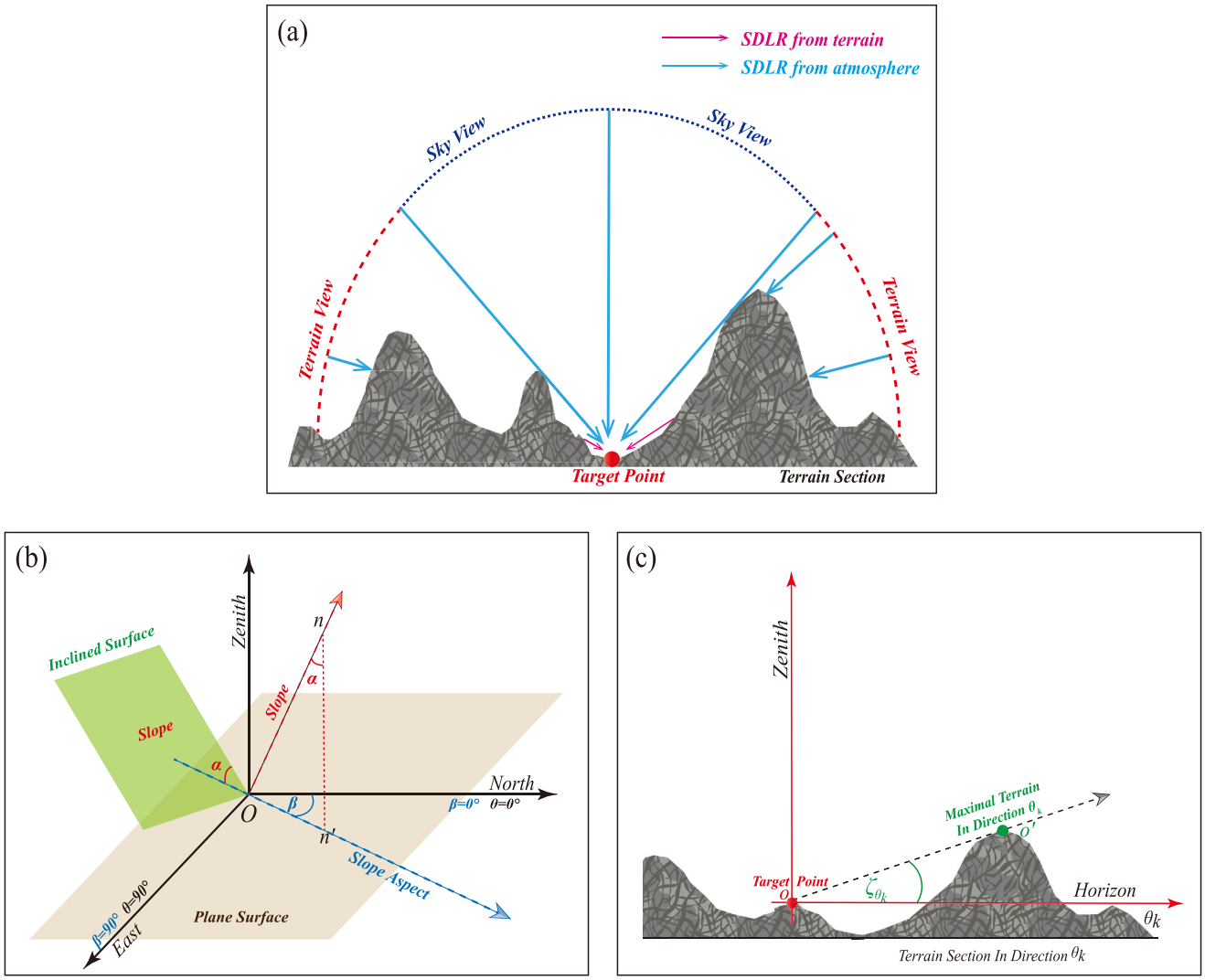

Figure 1. Illustration of the surface downwelling long-wave radiation components over the rugged surface (a); the slope (b); and the maximum elevation angle (c).

(Oliphant et al., 2003; Sicart et al., 2006). The sky view factor (*SKV*) is used to represent the 3-dimensional openness of the sky and determines the ratio of the SDLR from the atmosphere in the total SDLR (Figure 1a). The (1-*SKV*) is the terrain view factor and determines the ratio of the SDLR from the topography in the total SDLR. The mountain radiation theory has been widely applied in the previous studies, which not only improved the accuracy of calculated SDLR over the rugged areas but also refined the simulation of the SDLR related processes, such as the snow cover, the glacier melting, and the hydrological cycle (Duguay, 1993; Jiskoot & Mueller, 2012; Marks & Dozier, 1979; Olyphant, 1986; Robledano et al., 2022; Sicart et al., 2006; Webster et al., 2017). The main shortcoming of these studies is the assumption that the long-wave radiation fluxes emitted from the surrounding terrain are isotropic (Adams et al., 2011; Sicart et al., 2006). The isotropic assumption leads to the uncertainty of estimating the long-wave radiation emitted from the surrounding terrain. In reality, the long-wave radiation fluxes emitted from the surrounding terrain are anisotropic. For example, the surface temperature and emitted long-wave radiation at the sunny part of the crater differs from those at the shading part of the crater (Whiteman & Hoch, 2010).

2.2. Explicit Calculation of SDLR Over Rugged Surface Based on Mountain Radiation Theory

Over the plane surface, the clear-sky SDLR ($L_{p\downarrow}$) is calculated by equation provided by Niemelä et al. (2001) as follows:

$$L_{p\downarrow} = \varepsilon_a \sigma T_a^4 \tag{1}$$

Where $\varepsilon_a = 1.24 \cdot \left(\frac{e_a}{T_a}\right)^{\frac{1}{7}}$ (Brutsaert, 1975), e_a, T_a, and $\sigma = 5.67 \times 10^{-8}$ W · m^{-2} K^{-4} (Carmona et al., 2014) are the clear-sky atmospheric effective emissivity, the 2 m water vapor pressure, the near surface air temperature (2.0 m above ground surface), and the Stefan-Boltzmann constant, respectively.

The clear-sky SDLR over the rugged surface ($L_{t\downarrow}$) can be calculated by the equation of Duguay (1995) and Robledano et al. (2022):

$$L_{t\downarrow} = SKV \cdot L_{p\downarrow} + (1 - SKV) \cdot L_{\text{sur}} \tag{2}$$

where $SKV \cdot L_p\downarrow$ and $(1 - SKV) \cdot L_{\text{sur}}$ are the SDLR from the atmosphere and the received long-wave radiation emitted from the surrounding terrains, respectively. The L_{sur} is the long-wave radiation fluxes emitted by the surrounding terrain and calculated by $L_{\text{sur}} = \overline{\varepsilon}_{\text{sur}} \sigma \overline{T}_{\text{sur}}^4$, where $\overline{\varepsilon}_{\text{sur}}$ and $\overline{T}_{\text{sur}}$ are the surface emissivity (ε_s) and temperature (T_s) regionally averaged over the neighboring sub-grids within the radius of 1 km.

Jiao et al. (2019) recommends the *SKV* to be calculated by the Equation of Dozier and Frew (1990):

$$SKV = \frac{1}{N} \sum_{k=1}^{N} \left[\sin \alpha \cdot \cos(\theta_k - \beta) \left(\frac{\pi}{2} - \zeta_{\theta_k} - \sin \zeta_{\theta_k} \cdot \cos \zeta_{\theta_k} \right) + \cos \alpha \cdot \cos^2 \zeta_{\theta_k} \right] \tag{3}$$

where α and β are the terrain slope and the slope orientation (Figure 1b), θ_k is the azimuth angle in the kth direction, ζ_{θ_k} is the maximal terrain elevation angle in the direction θ_k (the angle between the line oo′ and the horizontal line in Figure 1c). As shown in Figure 1b, the terrain slope α is defined as the angle between the inclined surface (the normal line of the inclined surface) and the horizontal surface (the zenith). The terrain slope aspect β is defined as the angle between the north direction and the projection of the normal line of the slope on the horizontal surface. The α and β are the functions of the gradient of altitude ($\frac{\partial Z}{\partial x}$, $\frac{\partial Z}{\partial y}$) (Sharpnack & Akin, 1969; Zhou & Liu, 2004):

$$\alpha = \tan^{-1} \sqrt{\left(\frac{\partial Z}{\partial x}\right)^2 + \left(\frac{\partial Z}{\partial y}\right)^2} \tag{4}$$

$$\beta = \begin{cases} \frac{\pi}{2} - \tan^{-1}\left(\frac{\partial Z}{\partial y} \Big/ \frac{\partial Z}{\partial x}\right), & if \ \frac{\partial Z}{\partial x} < 0 \\ \frac{3\pi}{2} - \tan^{-1}\left(\frac{\partial Z}{\partial y} \Big/ \frac{\partial Z}{\partial x}\right), & if \ \frac{\partial Z}{\partial x} > 0 \\ \text{undef}, & if \ \frac{\partial Z}{\partial x} = 0 \text{ and } \frac{\partial Z}{\partial y} = 0 \\ 0, & if \ \frac{\partial Z}{\partial x} = 0 \text{ and } \frac{\partial Z}{\partial y} < 0 \\ \pi, & if \ \frac{\partial Z}{\partial x} = 0 \text{ and } \frac{\partial Z}{\partial y} > 0 \end{cases} \tag{5}$$

where the altitude gradient is the third-order finite difference of the altitude Z from the digital elevation model (DEM) data (Jarvis et al., 2008) with the horizontal resolution of 3″ (~90 m): $\begin{cases} \frac{\partial Z}{\partial x} = \frac{(Z_{m+1,n+1} - Z_{m-1,n+1}) + (Z_{m+1,n} - Z_{m-1,n}) + (Z_{m+1,n-1} - Z_{m-1,n-1})}{6\Delta x} \\ \frac{\partial Z}{\partial y} = \frac{(Z_{m+1,n+1} - Z_{m+1,n-1}) + (Z_{m,n+1} - Z_{m,n-1}) + (Z_{m-1,n+1} - Z_{m-1,n-1})}{6\Delta y} \end{cases}$. The subscript m (n) and the item Δx (Δy) are the grid number and the horizontal resolution of the grid in the west-east (north-south) direction of the

DEM data. The α varies from 0 to $\frac{\pi}{2}$. Both the β and the θ vary from 0 to 2π. The value 0, $\frac{\pi}{2}$, π, and $\frac{3\pi}{2}$ of the β (θ) are the north, east, south, and west aspect (direction), respectively.

By considering the effect of area variation due to the rugged terrain, the grid-cell-mean flux is calculated by $L_g = \frac{1}{n}\sum_{i=1}^{i=n}(L_i \cdot \sec\alpha_i)/\frac{1}{n}\sum_{i=1}^{i=n}\sec\alpha_i$ (Huang et al., 2022). The L_g, L_i, and α_i are the grid-cell-mean flux, sub-grid scale flux, and sub-grid scale terrain slope. For a model grid g with N rugged sub-grids, the clear-sky SDLR is explicitly calculated by:

$$L_{t,g\downarrow} = \frac{1}{N}\sum_{i=1}^{i=N}(SKV_i \cdot L_{p,i\downarrow} \cdot \sec\alpha_i + (1 - SKV_i) \cdot L_{sur,i} \cdot \sec\alpha_i)/\frac{1}{N}\sum_{i=1}^{i=N}\sec\alpha_i \quad (6)$$

2.3. 3DSTLRE Parameterization Scheme

Previous studies indicate that the variation of the *SKV* is much more important to determine the STLRE than the variation of the long-wave radiation fluxes emitted from the adjacent topographies (Duguay, 1995; Sicart et al., 2006). Therefore, we hypothesize that the thermal conditions of the sub-grids i are homogeneous within the model grid g with the horizontal resolutions of several kilometers to tens of kilometers ($T_{a,i} \doteq T_{a,g}$, $\varepsilon_{a,i} \doteq \varepsilon_{a,g}$, $\overline{T}_{\mathrm{sur},i} \doteq T_{s,g}$, and $\overline{\varepsilon}_{\mathrm{sur},i} \doteq \varepsilon_{s,g}$). In other words, assuming the differences of the plane surface long-wave radiation fluxes calculated between the grid and its sub-grids to be neglectable ($L_{p,i\downarrow} \doteq L_{p,g\downarrow}$, $L_{\mathrm{sur},i} \doteq L_{p,g\uparrow} = \varepsilon_{s,g}\sigma T_{s,g}^4$), then Equation 6 is converted to Equation 7:

$$L_{t,g\downarrow} = L_{p,g\downarrow} \cdot C_1 + L_{p,g\uparrow} \cdot C_2 \quad (7)$$

$$C_1 = \left(\sum_{i=1}^{i=N} SKV_i \cdot \sec\alpha_i\right)/\left(\sum_{i=1}^{i=N}\sec\alpha_i\right) \quad (8)$$

$$C_2 = \left[\sum_{i=1}^{i=N}(1 - SKV_i) \cdot \sec\alpha_i\right]/\left(\sum_{i=1}^{i=N}\sec\alpha_i\right) \quad (9)$$

The 3DSTLRE scheme is conducted in three steps: (a) Calculate the sub-grid scale α and *SKV* based on the high-resolution DEM data according to Equations 3–5. (b) Calculate the grid-scale terrain modification factors C_1 and C_2 based on the sub-grid scale α and *SKV* according to Equations 8 and 9. (c) Use the grid-scale terrain correction factors C_1, C_2 ($C_1 + C_2 = 1$) and the grid-scale surface long-wave radiation ($L_{p,g\downarrow}$ and $L_{p,g\uparrow}$) simulated by the plane-parallel scheme to calculate the grid-scale SDLR ($L_{t,g\downarrow}$) with the consideration of the 3DSTLRE according to the Equation 7.

When 3DSTSRE scheme is implemented in numerical models under all-sky conditions, the grid-scale downward and upward surface long-wave radiation fluxes ($L_{p,g\downarrow}$ and $L_{p,g\uparrow}$) in Equation 7 are provided by the plane-parallel radiative transfer module and the land surface module of the numerical models. After the step 3, the grid-scale downward surface long-wave radiation flux with the 3DSTLRE ($L_{t,g\downarrow}$) replaces the $L_{p,g\downarrow}$ to participate the sub-sequent calculations in the numerical model. The computation costs are primarily in the step 1. Both the steps 1 and 2 are prepared before the model run. The step 3 during the model integration does not put computation burden to the model. The 3DSTLRE scheme also has the advantage of strong portability because the calculation of 3DSTLRE scheme (Equation 7) during model run is quite simple. Equation 7 can be calculated in the atmospheric module or land surface module of the numerical model.

3. Data, Experimental Design, and Evaluation Metrics

3.1. Data

1. The Shuttle Radar Topography Mission (SRTM) Digital Elevation Database Version 4.1 (Jarvis et al., 2008) with a horizontal resolution of 3″ (~90 m) are used to calculate the sub-grid α, β, and *SKV*.
2. The Terra Moderate Resolution Imaging Spectroradiometer (MODIS) product (MOD11A1v061, Wan et al., 2021a) with a horizontal resolution of 1 km in 2012 offers the daily ground emissivity of bands 31 and 32. The missing values of the MOD11A1v061 product are filled by the 8 days average ground emissivity of the MODIS product (MOD11A2v061, Wan et al., 2021b) with a horizontal resolution of 1 km and the monthly ground emissivity of the MODIS product (MOD11C3v061, Wan et al., 2021c) with a horizontal resolution of

0.05°. Then the daily broadband ground emissivity ε_s with a horizontal resolution of 1 km are obtained with the processed daily emissivity of band 31 (ε_{31}, wavelength 10.780–11.280 nm) and band 32 (ε_{32}, wavelength 11.770–12.270 nm) by Liang (2003):

$$\varepsilon_s = 0.273 + 1.778\varepsilon_{31} - 1.807\varepsilon_{31}\varepsilon_{32} - 1.037\varepsilon_{32} + 1.774\varepsilon_{32}^2 \tag{10}$$

3. The daily near surface air temperature at height of 2.0 m above ground surface is averaged by the daily maximum and minimum near surface temperature data based on the combination of station-based measurements and satellite observation with a horizontal resolution of 1 km in 2012 (Zhang, Zhou, Zhao, et al., 2022).
4. The daily land surface temperature is averaged by the daytime and nighttime land surface temperature data set based on the satellite observation with a horizontal resolution of 1 km in 2012 (Zhang, Zhou, Zhu, et al., 2022).
5. The hourly 2 m dewpoint temperature from the fifth generation European Centre for Medium-Range Weather Forecasts (ECWMF) land surface reanalysis (ERA5-Land) reanalysis with a horizontal resolution of 0.1° (Muñoz Sabater, 2019) are used to calculate the hourly near surface water vapor pressure following Murray (1967):

$$e_a = \begin{cases} 6.1078 \cdot \exp\left[\dfrac{21.8745584(T_d - 273.16)}{T_d - 7.66}\right] & over\ the\ ice \\ 6.1078 \cdot \exp\left[\dfrac{17.2693882(T_d - 273.16)}{T_d - 35.86}\right] & over\ the\ water \end{cases} \tag{11}$$

where e_a and T_d are the 2 m water vapor pressure and 2 m dewpoint temperature with the units of hPa and K. The hourly water vapor pressure data are averaged to the daily water vapor pressure data.

Due to lack of the temperature and emissivity data which share the same horizontal resolution with the SRTM data (3″, ~90 m), for a compromise, the temperature and emissivity data with the horizontal resolution of 1 km are processed to the resolution of 3″ by the following methods. The calculated broadband emissivity and water vapor pressure data are interpolated to the grid of the SRTM data by the bilinear interpolation (Shi et al., 2014). The temperature is calculated to the grid of the SRTM data by $T_z = \overline{T} - 0.0065\left(Z - \overline{Z}\right)$ (Dozier & Outcalt, 1979). $\overline{T}$ is the temperature with the horizontal resolution of 1 km. Z is the elevation with the horizontal resolution of 3″. $\overline{Z}$ is the elevation with the horizontal resolution of 1 km averaged from Z of SRTM data with the resolution of 3″ (~90 m). The unit of elevation is meter. Then the clear-sky atmospheric effective emissivity ε_a is estimated by $\varepsilon_a = 1.24 \cdot \left(\frac{e_a}{T_a}\right)^{\frac{1}{7}}$ with the processed air water vapor pressure and air temperature at the horizontal resolution of 3″.

3.2. Experimental Design

The global *SKV* and α with the horizontal resolution of 3″ are shown in Figures 2a and 2c. The TP owns the smallest *SKV* and largest α and is one of the regions with the most rugged topography in the world. Figures 2b and 2d show that the most complex terrains are located over the western TP, the southeastern TP, and the south edge of the TP. The topographies in the Qiangtang Plateau are moderately rugged while the topographies over the Gangetic Plain are quite plane. Thus, the region (70°E ~ 105°E, 25°N ~ 40N°) shown in Figures 2b and 2d owns abundant topographic features, which offers a suitable scenario for evaluating the 3DSTLRE scheme.

As shown in Table 2, three experiments named EXPL, PARA_Terrain, and PARA_Plane are carried out in this study. In the EXPL experiment, the daily clear-sky atmospheric effective emissivity, broadband ground emissivity, near surface air temperature, and ground surface temperature with the horizontal resolution of 3″ are used to explicitly calculate the daily SDLR fluxes at the sub-grids with the horizontal resolution of 3″. Then the daily SDLR fluxes with the horizontal resolution of 3″ are averaged to the model grids with the horizontal resolutions of 0.025°, 0.05°, 0.1°, 0.2°, 0.4°, and 0.8° by Equation 6. The PARA_Plane experiment calculates the grid scale daily SDLR fluxes over the idealized plane surface by Equation 1 over the model grids with the horizontal resolutions of 0.025°, 0.05°, 0.1°, 0.2°, 0.4°, and 0.8°. The PARA_-Terrain experiment calculates the grid scale daily SDLR flux with rugged sub-grids according to

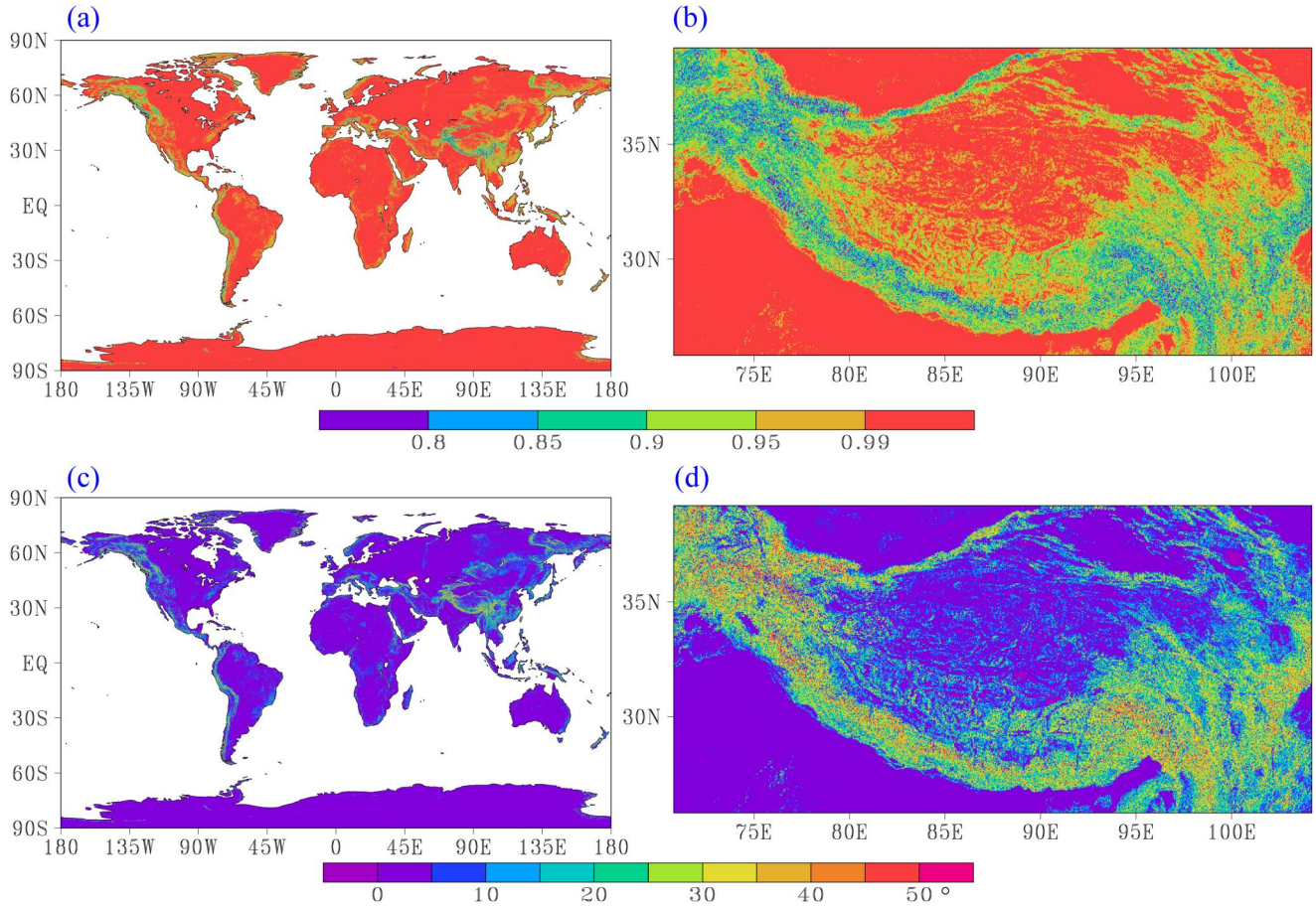

Figure 2. The sky view factor (a), (b) and slope (c), (d) of sub-grid scale terrain with the horizontal resolution of 3″ over the world (a), (c) and the testing field (b), (d).

Equation 7. The grid scale ground surface temperature ($T_{s,g}$), near surface temperature ($T_{a,g}$), and ground surface broadband emissivity ($\varepsilon_{s,g}$) in the PARA_Plane and PARA_Terrain experiments are regionally averaged from the daily clear-sky atmospheric effective emissivity, broadband ground emissivity, near surface air temperature, and ground surface temperature with the horizontal resolution of 3″ to each model

Table 2
Experimental Design

Experiment name	Calculation method	Resolution
EXPL	Explicitly calculate the daily SDLR fluxes at the grid of the SRTM data using the daily clear-sky atmospheric effective emissivity, broadband ground emissivity, near surface air temperature, and ground surface temperature with the horizontal resolution of 3″ according to Equation 6.	3″
PARA_Plane	Average the daily clear-sky atmospheric effective emissivity, broadband ground emissivity, near surface air temperature, and ground surface temperature with the horizontal resolution of 3″ to the grids with the different resolutions. Then use these average data to calculate grid scale daily SDLR fluxes according to Equation 1, which represents the model radiation scheme without considering the 3DSTLRE.	0.025°, 0.05°, 0.1°, 0.2°, 0.4°, and 0.8°
PARA_Terrain	Average the daily clear-sky atmospheric effective emissivity, broadband ground emissivity, near surface air temperature, and ground surface temperature with the horizontal resolution of 3″ to the grids with the different resolutions. Then use these average data to calculate grid-scale daily SDLR fluxes according to Equation 7 over the surface with the correction factor calculated by Equations 8 and 9, which represents the model radiation scheme adopting the 3DSTLRE.	0.025°, 0.05°, 0.1°, 0.2°, 0.4°, and 0.8°

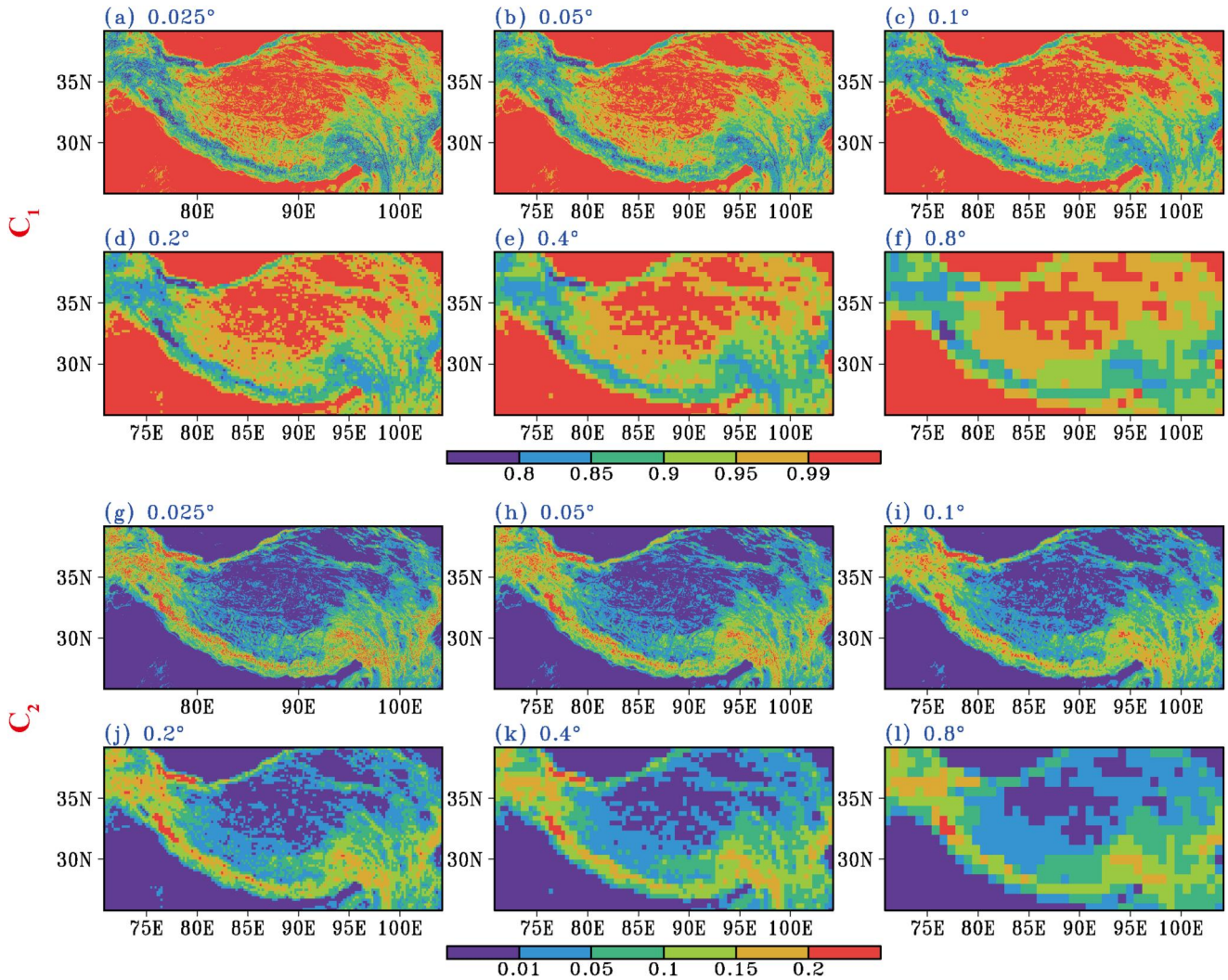

Figure 3. 3DSTLRE correction factor C_1 (a–f) and C_2 (g–l) in the grids with the horizontal resolutions of 0.025°, 0.05°, 0.1°, 0.2°, 0.4°, and 0.8°.

grid. Figure 3 shows the grid scale correction factors C_1 and C_2 with the different horizontal resolutions. Smaller (larger) value of correction factor C_1 (C_2) means that the long-wave radiation from the atmosphere (surrounding terrain) accounts less (more) in the grid scale SDLR flux, which indicates the grid-cell mean SDLR are more largely regulated by the sub-grid topographies.

3.3. Evaluation Metrics

The clear-sky daily SDLR fluxes calculated in the EXPL experiment are upscaled to the model grids with the horizontal resolutions ranging from 0.025° to 0.8° by Equation 6, which are treated as the "true value" in this study. The smaller (larger) differences of the SDLR flux between the PARA_Terrain and EXPL experiments (between the PARA_Plane and PARA_Terrain experiments) indicate the better performance of the 3DSTLRE scheme (greater importance of the 3DSTLRE). Compared to the EXPL experiment results which are treated as true values, the normalized mean absolute error (NMAE), error, and relative error of the PARA_Terrain experiment produced SDLR fluxes are used to evaluate the performance of the 3DSTLRE scheme. The differences of the SDLR fluxes between the PARA_Plane and PARA_Terrain experiments are used to assess the importance of the 3DSTLRE.

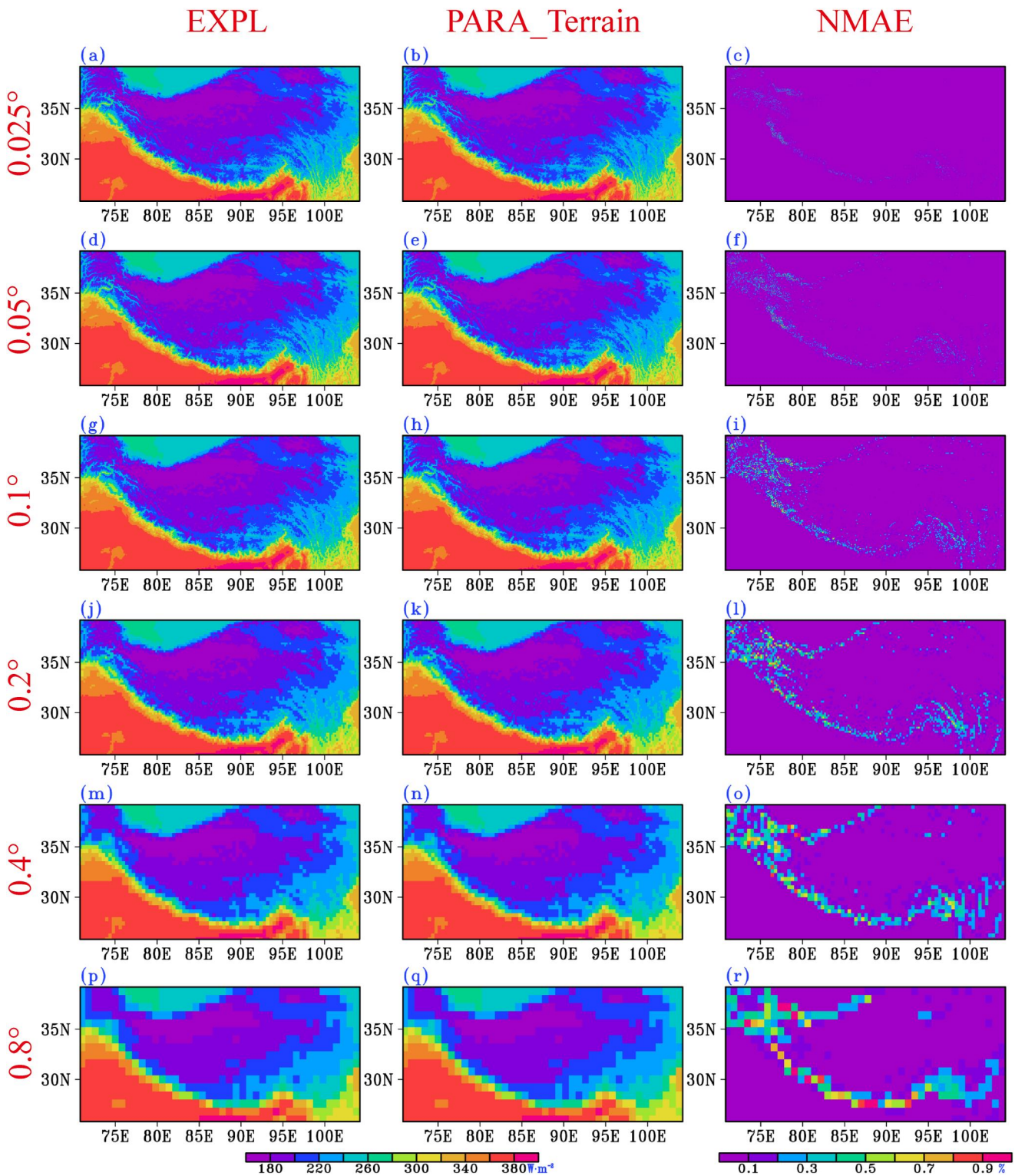

Figure 4. The surface downwelling long-wave radiation (SDLR) fluxes over 2012 in the EXPL (a, d, g, j, m, p) and PARA_Terrain (b, e, h, k, n, q) experiments and the normalized mean absolute error (NMAE, c, f, i, l, o, r) of the daily SDLR fluxes over 2012 in the experiment PARA_Terrain against the EXPL results with the horizontal resolution of 0.025°, 0.05°, 0.1°, 0.2°, 0.4°, and 0.8°.

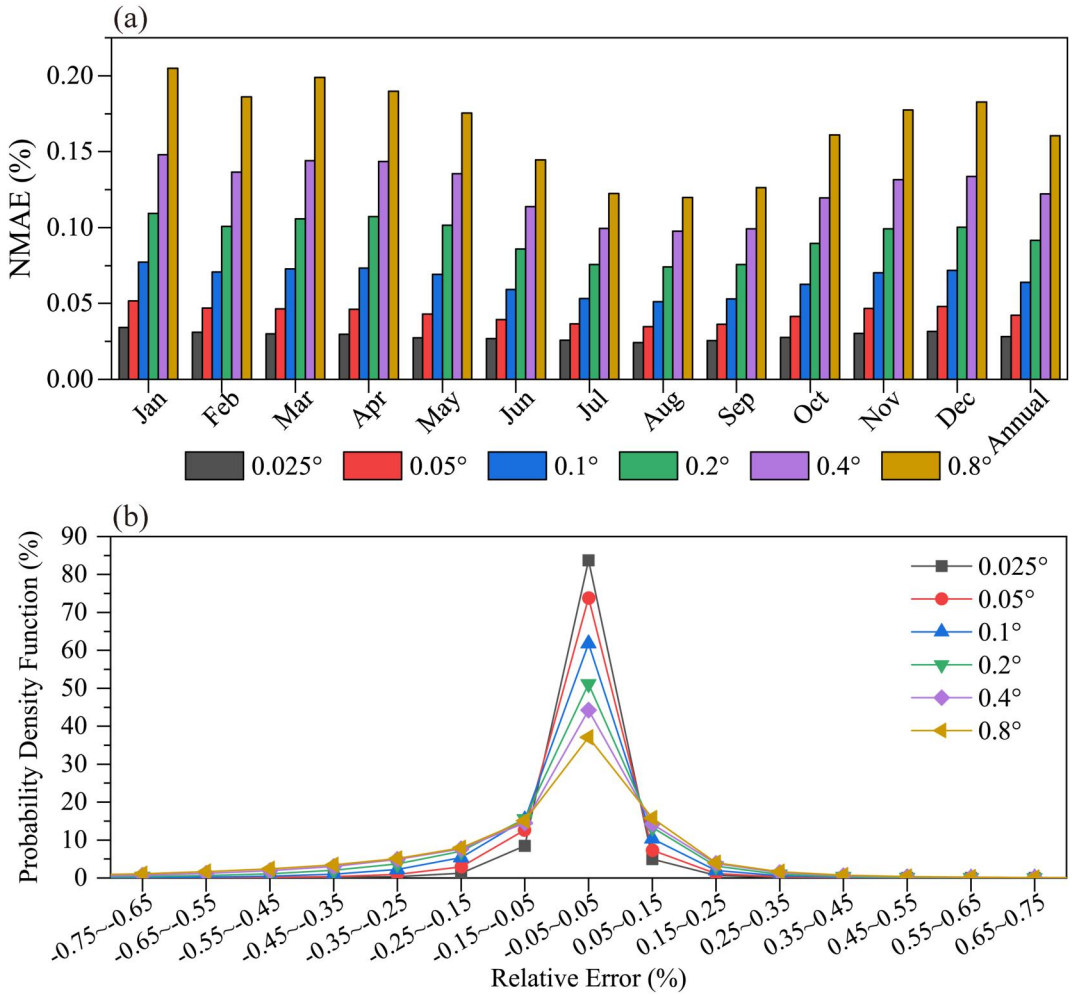

Figure 5. (a) The normalized mean absolute error of the daily surface downwelling long-wave radiation (SDLR) fluxes over months and whole year of 2012 from the PARA_Terrain experiment against the EXPL results and (b) the probability density function of the relative error of the daily SDLR fluxes in 2012 at the grids with the 3DSTLRE correction factor C_1 less than or equal to 0.99 in the experiment PARA_Terrain with the horizontal resolution of 0.025°, 0.05°, 0.1°, 0.2°, 0.4°, and 0.8°.

4. Results

4.1. Accuracy of the 3DSTLRE Parameterization Scheme

Figure 4 shows the NMAE of the daily clear-sky SDLR flux in the PARA_Terrain experiment throughout 2012 over the testing field. Most of the model grids with different horizontal resolutions have the NMAE of the simulated SDLR flux within 0.9%. Although the NMAE of the SDLR fluxes increases with the horizontal resolution of the grids decreasing from 0.025° to 0.8°, the NMAE of the SDLR fluxes in the grids with the horizontal resolutions of 0.8° are still acceptable.

The correction factor C_1 can be treated as the *SKV* at model grid scale. Smaller correction factor C_1 indicates the grid has stronger STLRE and receives less (more) SDLR from the atmosphere (terrain). The grid with the correction factor $C_1 > 0.99$ has very flat terrain and extremely weak STLRE, thus these grids with the correction factor $C_1 > 0.99$ are excluded in the following assessment. Figure 5a shows the NMAE of the daily clear-sky SDLR flux in different months and whole year of 2012 in the PARA_Terrain experiment at the grids with the correction factor $C_1 \leq 0.99$. Similar to those in Figure 4, the NMAE of SDLR fluxes increase along the decrease of the model horizontal resolutions. All the NMAE of SDLR simulation with different horizontal resolutions in different months are less than 0.25%. Therefore, the performance of 3DSTLRE scheme is stable and favorable throughout the year in the model grids with different horizontal resolutions. Figure 5b shows that 99.1%, 97.8%,

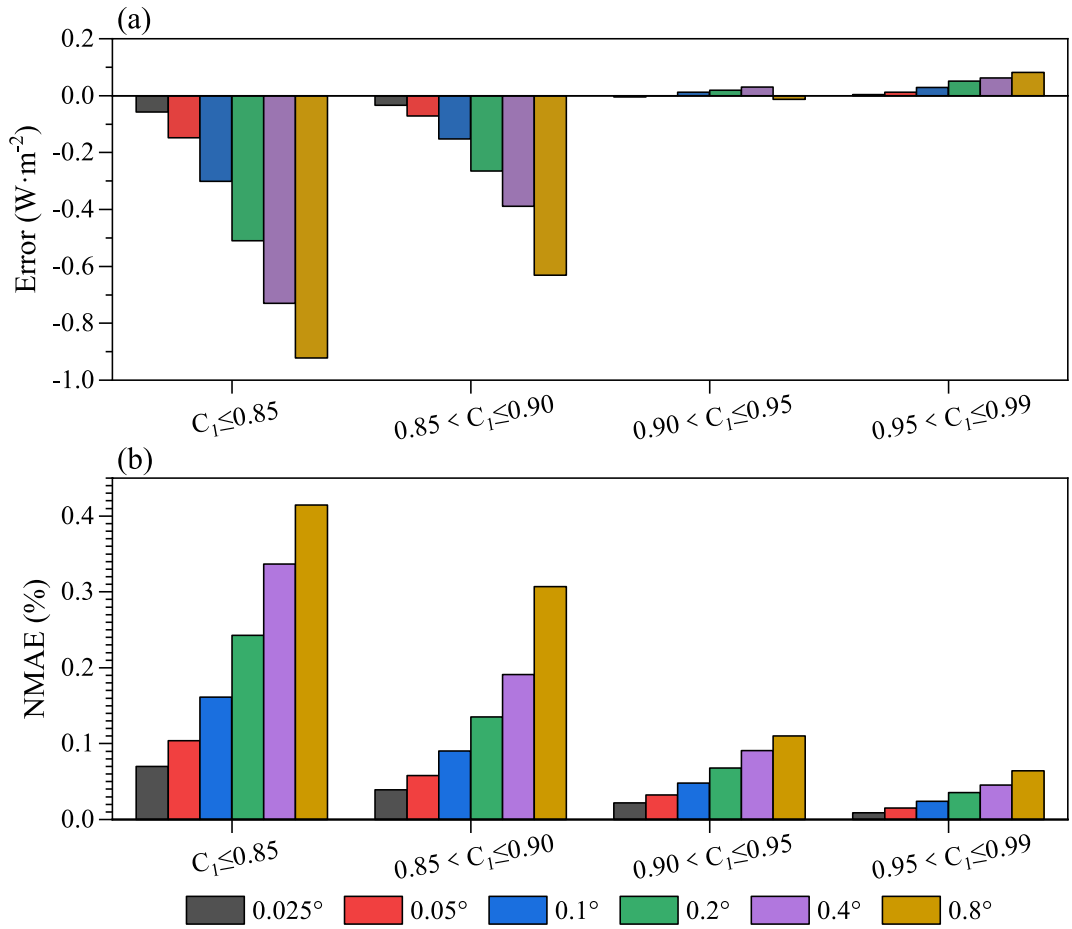

Figure 6. The error and normalized mean absolute error of the daily surface downwelling long-wave radiation fluxes at the grids with different values of the correction factor C_1 over 2012 in the PARA_Terrain experiment against the EXPL results with the horizontal resolution of 0.025°, 0.05°, 0.1°, 0.2°, 0.4°, and 0.8°.

94.9%, 90.2%, 84.4%, and 79.9% of the samples over the rugged terrain areas have the relative error of the daily SDLR fluxes within ±0.25% in the PARA_Terrain experiment with the horizontal resolution of 0.025°, 0.05°, 0.1°, 0.2°, 0.4°, and 0.8°, respectively. The probability density functions (PDF) of the relative error in the experiments with the different horizontal resolutions all follow the normal distribution with the peak of PDF at the relative error of −0.05~0.05%, indicating the similar probability of positive relative error and negative relative error and the good performance of the 3DSTLRE scheme.

To assess the performance of the 3DSTLRE scheme over the model grids with different complexity of sub-grid topography, the error and NMAE of the daily clear-sky SDLR fluxes over the model grids with different values of the correction factor C_1 are calculated and shown in Figure 6. The error and NMAE of the SDLR fluxes over the different grids increase along the decrease of the correction factor C_1 and grid horizontal resolution. The 3DSTLRE scheme has the largest uncertainty over the grids with fine resolution and high complexity of sub-grid topography. But even over the grids with a horizontal resolution of 0.8° and very rugged sub-grid topography (the correction factor $C_1 \leq 0.85$), the NMAEs (errors) of the daily SDLR fluxes simulated by the PARA_Terrain are less than 0.5% (within 1.0 $W \cdot m^{-2}$), indicating that the 3DSTLRE scheme has good performance and is portable to the models with different horizontal resolutions. Overall, the 3DSTLRE scheme shows high accuracy under the different conditions of grid horizontal resolution, time of the year, and sub-grid terrain complexity (Figures 3–6).

4.2. Importance of 3DSTLRE

Figure 7 shows the annual mean differences and relative differences of the daily clear-sky SDLR fluxes between the PARA_Plane and PARA_Terrain experiments throughout 2012. The mean differences of the simulated daily

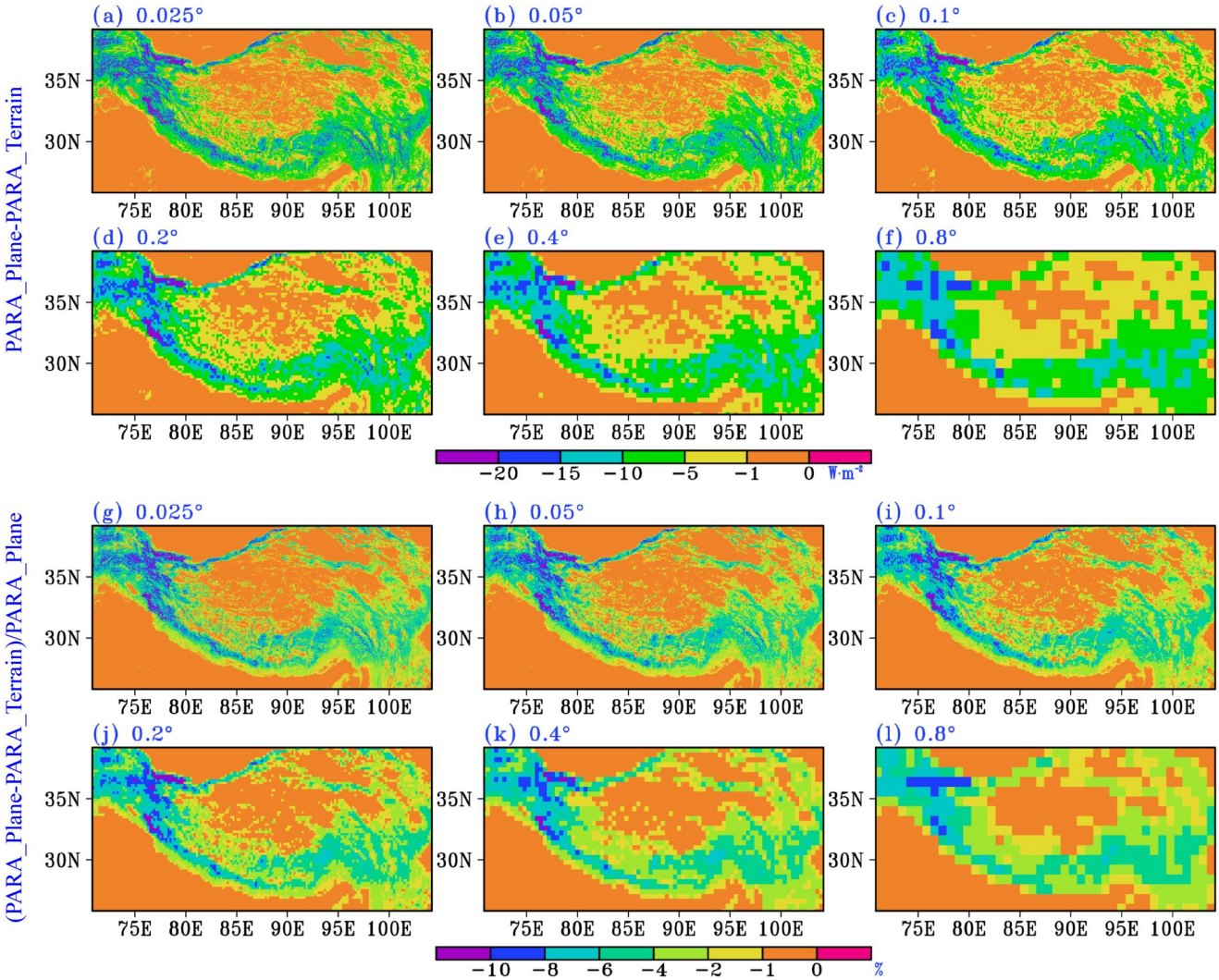

Figure 7. The mean difference (a–f) and relative difference (g–l) of the daily surface downwelling long-wave radiation fluxes over 2012 between the PARA_Plane and PARA_Terrain experiments with the horizontal resolution of 0.025°, 0.05°, 0.1°, 0.2°, 0.4°, and 0.8°.

SDLR fluxes between the PARA_Plane and the PARA_Terrain experiments over most of the rugged areas range from −20 to −5 W · m^{-2} at the horizontal resolution ranging from 0.025° to 0.8° (Figures 7a–7f). The differences increase with the sub-grid terrain complexity (the decrease of the correction factor C_1). Neglecting the 3DSTLRE tends to underestimate the SDLR flux over the rugged areas and the underestimation increases with the sub-grid terrain complexity. The mean relative underestimations of the SDLR fluxes in the PARA_Plane and the PARA_Terrain experiments are within 4% and 10% over most of rugged areas and exceed 10% over the grids in the western TP with the high horizontal resolution (Figures 7g–7l).

Figure 8 shows that the PARA_Plane experiment mainly underestimates the daily SDLR fluxes over the rugged area. The differences of the calculated SDLR between the PARA_Plane and PARA_Terrain experiments are larger when the horizontal resolution of the grid is higher (Figure 8a). About 1% and 10% of the samples at different horizontal resolutions show that the relative difference of the daily SDLR fluxes between the PARA_Plane and PARA_Terrain experiments are less than −13% and −8%, respectively (Figure 8b).

The differences of the SDLR fluxes between the PARA_Terrain and PARA_Plane experiments regionally averaged over the grids with the correction factor $C_1 \leq 0.99$ are shown in Figure 9. The differences vary from −9 to −4 W · m^{-2} in all months. The differences are relatively larger in the winter half year and at the model grids with higher horizontal resolution. The SDLR underestimations of plane-parallel scheme without the 3DSTLRE

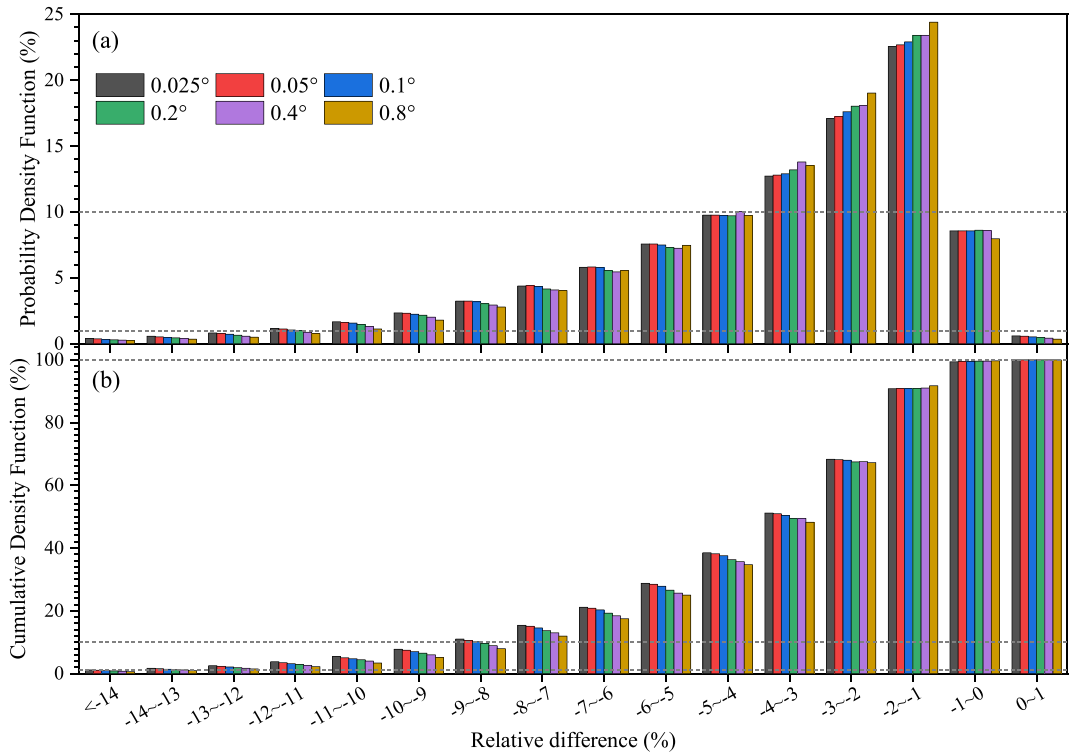

Figure 8. The probability density function (a) and cumulative density function (b) of the relative difference of the daily surface downwelling long-wave radiation fluxes at the grids with the correction factor $C_1 \leq 0.99$ over 2012 between the PARA_Plane and PARA_Terrain experiments with the horizontal resolution of 0.025°, 0.05°, 0.1°, 0.2°, 0.4°, and 0.8°.

over the areas with complex terrain in the winter half year are relatively larger, and underestimations increase with the model horizontal resolution and sub-grid terrain complexity (Figures 8 and 9). Overall, as shown in Figures 7–9, the larger biases will be generated in the areas with higher horizontal resolution and more rugged sub-grid scale topography in the cold months due to neglecting the 3DSTLRE.

5. Conclusion and Discussion

The long-wave radiation fluxes considerably affected by topography over rugged areas are important to the land-surface processes. However, the state-of-art numerical models lack the parameterization scheme to describe the

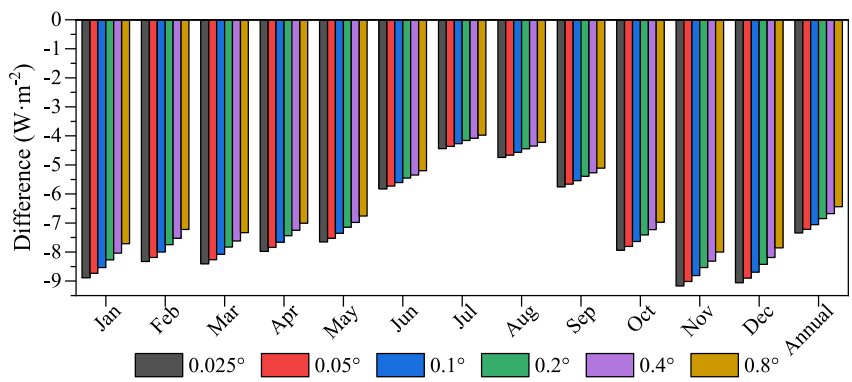

Figure 9. The mean difference of the daily surface downwelling long-wave radiation fluxes at the grids with the correction factor $C_1 \leq 0.99$ in each month and the whole year of 2012 between the PARA_Plane and PARA_Terrain experiments with the horizontal resolution of 0.025°, 0.05°, 0.1°, 0.2°, 0.4°, and 0.8°.

STLRE, adding the uncertainty to the simulated SDLR. This study develops a clear-sky 3DSTLRE parameterization scheme under the isotropic assumption of sub-grid terrain long-wave radiation. Three experiments in 2012 are conducted to evaluate the 3DSTLRE scheme over the TP. The EXPL experiment explicitly calculates the SDLR flux on the sub-grids with the horizontal resolution of 3″ considering the 3DSTLRE and provides the base for evaluating the performance of the 3DSTLRE scheme. The PARA_Plane (PARA_Terrain) experiment calculates the SDLR flux on the model grids with the horizontal resolutions of 0.025°, 0.05°, 0.1°, 0.2°, 0.4°, and 0.8° without (with) the 3DSTLRE parameterization scheme. Conclusions can be drawn as follows:

The 3DSTLRE scheme uses the grid scale terrain modification factors to correct the SDLR fluxes calculated by the plane-parallel scheme during the model integration without adding the computation burden. It is applicable to the models with different horizontal resolutions and different sub-grid terrain complexity. The 3DSTLRE scheme can be flexibly carried out in the radiative transfer module of the atmospheric model or in the updating processes of atmospheric forcing in the land surface model.

The 3DSTLRE scheme can properly describe the impacts of the sub-grid terrain on the SDLR. Compared to the explicit calculations on the sub-grid of 3″, the NMAE of the daily clear-sky SDLR flux in the PARA_Terrain experiment are less than 0.9% over most of TP. At different model horizontal resolutions, the NMAE of the SDLR flux in the PARA_Terrain experiment over the model grids with grid-scale terrain correction factor $C_1 \leq 0.99$ are less than 0.25% in different months. The NMAE (error) increases with the decrease of horizontal resolution and increase of sub-grid terrain complexity, but the NMAE (error) is less than 0.5% (within 1.0 $W \cdot m^{-2}$) even over the grids with very coarse resolution and complex sub-grid topography. High accuracy of the 3DSTLRE parameterization is stable regardless of grid horizontal resolution, sub-grid terrain complexity, and time of the year.

The plane-parallel radiative scheme neglecting the 3DSTLRE would lead to underestimated SDLR flux over the rugged areas. At different horizontal resolutions, the mean underestimations (relative underestimations) of the clear-sky SDLR flux over most of TP calculated by the plane-parallel scheme range from -20 to -5 $W \cdot m^{-2}$ (4∼10%) and exceed 20 $W \cdot m^{-2}$ (10%) over western TP. About 1% and 10% of the samples at different horizontal resolutions exhibits that the relative difference of the daily SDLR fluxes between the PARA_Plane and PARA_Terrain experiments are less than -13% and -8%, respectively. The underestimation of SDLR simulated by the plane-parallel scheme is much larger at the model grids with higher horizontal resolution and more rugged sub-grid scale topography during the cold months.

It should be admitted that this study has the following deficiencies due to the objective restrictions: (a) the 3DSTLRE scheme is based on the isotropic assumption of the long-wave radiation emitted from the surrounding terrain, which neglects the differences of the thermodynamic property between the target point and its surrounding topography. (b) The diurnal variation of performance of the 3DSTLRE scheme is not discussed in this study due to the lack of hourly observed temperature and emissivity data with high resolution. (c) The near surface air temperature, ground surface temperature, emissivity, and water vapor pressure data with the horizontal resolution of 3″ are derived from the data with coarser resolutions, which may raise the uncertainty of the estimation. (d) The near surface atmosphere absorption of the thermal energy is neglected when calculate the long-wave radiation from the surrounding terrain. Besides, the performance of the 3DSTLRE scheme should be carefully checked when the scheme is implemented over the other regions.

Nonetheless, this study offers an effective and practicable choice for the numerical models to adopt the 3DSTLRE. Because the cloud radiative forcing has been accounted in the radiative transfer module, the sub-grid topographic radiative effects parameterization scheme developed under the clear-sky condition can be directly applied to the all-sky condition (Gu et al., 2012; Lee et al., 2013). Thus, the 3DSTLRE scheme developed here also can correct the SDLR flux from the radiative transfer module under the cloudy condition. When 3DSTLR scheme is implemented in numerical models under the all-sky conditions, the performance of the 3DSTLR scheme can be comprehensively evaluated with the observations. Future plans include comparing the differences of the theories based on the isotropic (Duguay, 1995; Robledano et al., 2022) and anisotropic assumptions of the terrain emitted long-wave radiation flux (Wu et al., 2019; Yan et al., 2020). Furthermore, our preliminary results show that the 3DSTLRE scheme improves the performance of the Regional Climate Model version 4 in simulating the SDLR and the performance of the 3DSTLRE scheme is stable in different years, which will be reported later.

Data Availability Statement

The data used in this study are listed as follows: (a) the SRTM Digital Elevation Database Version 4.1 with a horizontal resolution of 3″ (Jarvis et al., 2008); (b) the global data set of daily near surface temperature in 2012 with a horizontal resolution of 1 km (Zhang, Zhou, Zhao, et al., 2022); (c) the global seamless daily land surface temperature data set in 2012 with a horizontal resolution of 1 km (Zhang, Zhou, Zhu, et al., 2022); (d) the daily, 8 days average, and monthly ground surface band 31/32 emissivity of MOD11A1v061 (Wan et al., 2021a), MOD11A2v061 (Wan et al., 2021b), and MOD11C3v061(Wan et al., 2021c) from the MODIS data sets in 2012 with a horizontal resolution of 1 km, 1 km, and 0.05° respectively; (e) the hourly 2 m dewpoint temperature of ERA5-Land reanalysis in 2012 with a horizontal resolution of 0.1°(Muñoz Sabater et al., 2019).

Acknowledgments

This study is supported by the National Natural Science Foundation of China under Grant 42375157, the National Key RandD Program of China under Grant 2022YFC3080500, Open Research Fund Program of Plateau Atmosphere and Environment Key Laboratory of Sichuan Province (PAEKL-2023-K01), the CAS "Light of West China" Program (E129030101), the Jiangsu University "Blue Project" outstanding young teachers training object, the Jiangsu Collaborative Innovation Center for Climate Change, and the Postgraduate Research and Practice Innovation Program of Jiangsu Province (No. 124 in 2023). We appreciate the High Performance Computing Center of Nanjing University and the National Key Scientific and Technological Infrastructure project "Earth System Numerical Simulation Facility" (EarthLab) for providing us the computing resource. We are grateful to CIAT, NASA, ECWMF, and Zhang, Zhou, Zhao, et al. (2022), Zhang, Zhou, Zhu, et al. (2022) for allowing us to use their data sets. We show our warm appreciation and deepest respect to the four anonymous reviewers for their constructive suggestions to greatly improve the manuscript.

References

Adams, E., Slaughter, A., McKittrick, L., & Miller, D. (2011). Local terrain-topography and thermal-properties influence on energy and mass balance of a snow cover. *Annals of Glaciology*, *52*(58), 169–175. https://doi.org/10.3189/172756411797252257

Arnold, N. S., Rees, W. G., Hodson, A. J., & Kohler, J. (2006). Topographic controls on the surface energy balance of a high Arctic valley glacier. *Journal of Geophysical Research*, *111*(F2). https://doi.org/10.1029/2005jf000426

Arthur, R., Lundquist, K., Mirocha, J., & Chow, F. (2018). Topographic effects on radiation in the WRF model with the immersed boundary method: Implementation, validation, and application to complex terrain. *Monthly Weather Review*, *146*(10), 3277–3292. https://doi.org/10.1175/MWR-D-18-0108.1

Aubry-Wake, C., Zéphir, D., Baraer, M., McKenzie, J. M., & Mark, B. G. (2018). Importance of longwave emissions from adjacent terrain on patterns of tropical glacier melt and recession. *Journal of Glaciology*, *64*(243), 49–60. https://doi.org/10.1017/jog.2017.85

Brutsaert, W. (1975). On a derivable formula for long-wave radiation from clear skies. *Water Resources Research*, *11*(5), 742–744. https://doi.org/10.1029/WR011i005p00742

Carmona, F., Rivas, R., & Caselles, V. (2014). Estimation of daytime downward longwave radiation under clear and cloudy skies conditions over a sub-humid region. *Theoretical and Applied Climatology*, *115*(1), 281–295. https://doi.org/10.1007/s00704-013-0891-3

Chen, X., Liu, Y., & Wu, G. (2017). Understanding the surface temperature cold bias in CMIP5 AGCMs over the Tibetan Plateau. *Advances in Atmospheric Sciences*, *34*(12), 1447–1460. https://doi.org/10.1007/s00376-017-6326-9

Chen, Y.-W., Seiki, T., Kodama, C., Satoh, M., & Noda, A. T. (2018). Impact of precipitating ice hydrometeors on longwave radiative effect estimated by a global cloud-system resolving model. *Journal of Advances in Modeling Earth Systems*, *10*(2), 284–296. https://doi.org/10.1002/2017MS001180

Dozier, J., & Frew, J. (1990). Rapid calculation of terrain parameters for radiation modeling from digital elevation data. *IEEE Transactions on Geoscience and Remote Sensing*, *28*(5), 963–969. https://doi.org/10.1109/36.58986

Dozier, J., & Outcalt, S. I. (1979). An approach toward energy balance simulation over rugged terrain. *Geographical Analysis*, *11*(1), 65–85. https://doi.org/10.1111/j.1538-4632.1979.tb00673.x

Duguay, C. R. (1993). Modelling the radiation budget of alpine snowfields with remotely sensed data: Model formulation and validation. *Annals of Glaciology*, *17*, 288–294. https://doi.org/10.1017/s0260305500012982

Duguay, C. R. (1995). An approach to the estimation of surface net radiation in mountain areas using remote sensing and digital terrain data. *Theoretical and Applied Climatology*, *52*(1), 55–68. https://doi.org/10.1007/BF00865507

Fan, X., Gu, Y., Liou, K. N., Lee, W. L., Zhao, B., Chen, H., & Lu, D. (2019). Modeling study of the impact of complex terrain on the surface energy and hydrology over the Tibetan Plateau. *Climate Dynamics*, *53*(11), 6919–6932. https://doi.org/10.1007/s00382-019-04966-z

Feldman, D. R., Worden, M., Falco, N., Dennedy-Frank, P. J., Chen, J., Dafflon, B., & Wainwright, H. (2022). Three-dimensional surface downwelling longwave radiation clear-sky effects in the upper Colorado River Basin. *Geophysical Research Letters*, *49*(4). https://doi.org/10.1029/2021GL094605

Feng, L., & Zhang, Y. (2007). Impacts of the thermal effects of sub-grid orography on the heavy rainfall events along the Yangtze River Valley in 1991. *Advances in Atmospheric Sciences*, *24*(5), 881–892. https://doi.org/10.1007/s00376-007-0881-4

Gratton, D. J., Howarth, P. J., & Marceau, D. J. (1993). Using Landsat-5 thematic mapper and digital elevation data to determine the net radiation field of a Mountain Glacier. *Remote Sensing of Environment*, *43*(3), 315–331. https://doi.org/10.1016/0034-4257(93)90073-7

Gu, C., Huang, A., Wu, Y., Yang, B., Mu, X., Zhang, X., & Cai, S. (2020). Effects of subgrid terrain radiative forcing on the ability of RegCM4.1 in the simulation of summer precipitation over China. *Journal of Geophysical Research: Atmospheres*, *125*(12). https://doi.org/10.1029/2019jd032215

Gu, C., Huang, A., Zhang, Y., Yang, B., Cai, S., Xu, X., et al. (2022). The wet bias of RegCM4 over Tibet Plateau in summer reduced by adopting the 3D sub-grid terrain solar radiative effect parameterization scheme. *Journal of Geophysical Research: Atmospheres*, *127*(21). https://doi.org/10.1029/2022JD037434

Gu, Y., Liou, K. N., Lee, W. L., & Leung, L. R. (2012). Simulating 3-D radiative transfer effects over the Sierra Nevada Mountains using WRF. *Atmospheric Chemistry and Physics*, *12*(20), 9965–9976. https://doi.org/10.5194/acp-12-9965-2012

Hao, D., Bisht, G., Gu, Y., Lee, W. L., Liou, K. N., & Leung, L. R. (2021). A parameterization of sub-grid topographical effects on solar radiation in the E3SM Land Model (version 1.0): Implementation and evaluation over the Tibetan Plateau. *Geoscientific Model Development*, *14*(10), 6273–6289. https://doi.org/10.5194/gmd-14-6273-2021

Hauge, G., & Hole, L. R. (2003). Implementation of slope irradiance in Mesoscale Model version 5 and its effect on temperature and wind fields during the breakup of a temperature inversion. *Journal of Geophysical Research*, *108*(D2). https://doi.org/10.1029/2002jd002575

Hu, T., Cao, B., Du, Y., Li, H., Wang, C., Bian, Z., et al. (2017). Estimation of surface upward longwave radiation using a direct physical algorithm. *IEEE Transactions on Geoscience and Remote Sensing*, *55*(8), 4412–4426. https://doi.org/10.1109/TGRS.2017.2692261

Huang, A., Gu, C., Zhang, Y., Li, W., Zhang, L., Wu, Y., et al. (2022). Development of a clear-sky 3D sub-grid terrain solar radiative effect parameterization scheme based on the mountain radiation theory. *Journal of Geophysical Research: Atmospheres*, *127*(13). https://doi.org/10.1029/2022jd036449

Jarvis, A., Reuter, H. I., Nelson, A., & Guevara, E. (2008). The shuttle radar topography mission (SRTM) 90m digital elevation Database v4.1 [Dataset]. International Centre for Tropical Agriculture (CIAT). https://developers.google.com/earth-engine/datasets/catalog/CGIAR_SRTM90_V4

Jiao, Z.-H., & Mu, X. (2022). Global validation of clear-sky models for retrieving land-surface downward longwave radiation from MODIS data. *Remote Sensing of Environment*, *271*, 112903. https://doi.org/10.1016/j.rse.2022.112903

Jiao, Z.-H., Ren, H., Mu, X., Zhao, J., Wang, T., & Dong, J. (2019). Evaluation of four sky view factor algorithms using digital surface and elevation model data. *Earth and Space Science*, *6*(2), 222–237. https://doi.org/10.1029/2018EA000475

Jin, Z., Zhang, Y., Del Genio, A., Schmidt, G., & Kelley, M. (2019). Cloud scattering impact on thermal radiative transfer and global longwave radiation. *Journal of Quantitative Spectroscopy and Radiative Transfer*, *239*, 106669. https://doi.org/10.1016/j.jqsrt.2019.106669

Jiskoot, H., & Mueller, M. S. (2012). Glacier fragmentation effects on surface energy balance and runoff: Field measurements and distributed modelling. *Hydrological Processes*, *26*(12), 1861–1875. https://doi.org/10.1002/hyp.9288

Laguë, M. M., Bonan, G. B., & Swann, A. L. S. (2019). Separating the impact of individual land surface properties on the terrestrial surface energy budget in both the coupled and uncoupled land–Atmosphere System. *Journal of Climate*, *32*(18), 5725–5744. https://doi.org/10.1175/jcli-d-18-0812.1

Lee, W. L., Liou, K. N., & Hall, A. (2011). Parameterization of solar fluxes over mountain surfaces for application to climate models. *Journal of Geophysical Research*, *116*(D1), D01101. https://doi.org/10.1029/2010jd014722

Lee, W. L., Liou, K. N., & Wang, C. (2013). Impact of 3-D topography on surface radiation budget over the Tibetan Plateau. *Theoretical and Applied Climatology*, *113*(1), 95–103. https://doi.org/10.1007/s00704-012-0767-y

Li, J.-L. F., Waliser, D. E., Stephens, G., Lee, S., L'Ecuyer, T., Kato, S., et al. (2013). Characterizing and understanding radiation budget biases in CMIP3/CMIP5 GCMs, contemporary GCM, and reanalysis. *Journal of Geophysical Research: Atmospheres*, *118*(15), 8166–8184. https://doi.org/10.1002/jgrd.50378

Liang, S. (2003). Estimation of surface radiation budget: II. Longwave. In *Quantitative remote sensing of land surfaces* (pp. 345–397). https://doi.org/10.1002/047172372X.ch10

Ma, Q., Wang, K., & Wild, M. (2014). Evaluations of atmospheric downward longwave radiation from 44 coupled general circulation models of CMIP5. *Journal of Geophysical Research: Atmospheres*, *119*(8), 4486–4497. https://doi.org/10.1002/2013JD021427

Ma, X., Jin, J., Liu, J., & Niu, G. Y. (2019). An improved vegetation emissivity scheme for land surface modeling and its impact on snow cover simulations. *Climate Dynamics*, *53*(9), 6215–6226. https://doi.org/10.1007/s00382-019-04924-9

Manners, J., Vosper, S. B., & Roberts, N. (2012). Radiative transfer over resolved topographic features for high-resolution weather prediction. *Quarterly Journal of the Royal Meteorological Society*, *138*(664), 720–733. https://doi.org/10.1002/qj.956

Marks, D., & Dozier, J. (1979). A clear-sky longwave radiation model for remote alpine areas. *Archiv für Meteorologie, Geophysik und Bioklimatologie, Serie B*, *27*(2), 159–187. https://doi.org/10.1007/BF02243741

Matzinger, N., Andretta, M., Gorsel, E. V., Vogt, R., Ohmura, A., & Rotach, M. W. (2003). Surface radiation budget in an Alpine valley. *Quarterly Journal of the Royal Meteorological Society*, *129*(588), 877–895. https://doi.org/10.1256/qj.02.44

Morcrette, J. J. (2002). The surface downward longwave radiation in the ECMWF forecast system. *Journal of Climate*, *15*(14), 1875–1892. https://doi.org/10.1175/1520-0442(2002)015<1875:Tsdlri>2.0.Co;2

Müller, M. D., & Scherer, D. (2005). A grid- and subgrid-scale radiation parameterization of topographic effects for mesoscale weather forecast models. *Monthly Weather Review*, *133*(6), 1431–1442. https://doi.org/10.1175/mwr2927.1

Muñoz Sabater, J. (2019). ERA5-Land hourly data from 1950 to present [Dataset]. Copernicus Climate Change Service (C3S) Climate Data Store (CDS). https://doi.org/10.24381/cds.e2161bac

Murray, F. W. (1967). On the computation of saturation vapor pressure. *Journal of Applied Meteorology and Climatology*, *6*(1), 203–204. https://doi.org/10.1175/1520-0450(1967)006<0203:OTCOSV>2.0.CO;2

Niemelä, S., Räisänen, P., & Savijärvi, H. (2001). Comparison of surface radiative flux parameterizations: Part I: Longwave radiation. *Atmospheric Research*, *58*(1), 1–18. https://doi.org/10.1016/S0169-8095(01)00084-9

Oliphant, A. J., Spronken-Smith, R. A., Sturman, A. P., & Owens, I. F. (2003). Spatial variability of surface radiation fluxes in mountainous terrain. *Journal of Applied Meteorology*, *42*(1), 113–128. https://doi.org/10.1175/1520-0450(2003)042<0113:Svosrf>2.0.Co;2

Olyphant, G. A. (1986). Longwave radiation in mountainous areas and its influence on the energy balance of Alpine snowfields. *Water Resources Research*, *22*(1), 62–66. https://doi.org/10.1029/WR022i001p00062

Panicker, A. S., Pandithurai, G., Safai, P. D., & Kewat, S. (2008). Observations of enhanced aerosol longwave radiative forcing over an urban environment. *Geophysical Research Letters*, *35*(4). https://doi.org/10.1029/2007GL032879

Pashiardis, S., Kalogirou, S. A., & Pelengaris, A. (2017). Characteristics of longwave radiation through the statistical analysis of downward and upward longwave radiation and inter-comparison of two sites in Cyprus. *Journal of Atmospheric and Solar-Terrestrial Physics*, *164*, 60–80. https://doi.org/10.1016/j.jastp.2017.08.007

Peng, Y., Zhao, J. Q., Sun, Z., Zhao, W., Wei, X., & Li, J. (2018). Sensitivity of dust radiative forcing to representation of aerosol size distribution in radiative transfer model. *Journal of Quantitative Spectroscopy and Radiative Transfer*, *219*, 292–303. https://doi.org/10.1016/j.jqsrt.2018.04.037

Plüss, C., & Ohmura, A. (1997). Longwave radiation on snow-covered mountainous surfaces. *Journal of Applied Meteorology*, *36*(6), 818–824. https://doi.org/10.1175/1520-0450-36.6.818

Robledano, A., Picard, G., Arnaud, L., Larue, F., & Ollivier, I. (2022). Modelling surface temperature and radiation budget of snow-covered complex terrain. *The Cryosphere*, *16*(2), 559–579. https://doi.org/10.5194/tc-16-559-2022

Shakespeare, C. J., & Roderick, M. L. (2022). Diagnosing instantaneous forcing and feedbacks of downwelling longwave radiation at the surface: A simple methodology and its application to CMIP5 models. *Journal of Climate*, *35*(12), 3785–3801. https://doi.org/10.1175/jcli-d-21-0865.1

Sharpnack, D. A., & Akin, G. (1969). An algorithm for computing slope and aspect from elevations. *Photogrammetric Engineering*, *35*(3), 247–248.

Shi, W., Wang, B., & Tian, Y. (2014). Accuracy analysis of digital elevation model relating to spatial resolution and terrain slope by bilinear interpolation. *Mathematical Geosciences*, *46*(4), 445–481. https://doi.org/10.1007/s11004-013-9508-8

Sicart, J. E., Pomeroy, J. W., Essery, R. L. H., & Bewley, D. (2006). Incoming longwave radiation to melting snow: Observations, sensitivity and estimation in Northern environments. *Hydrological Processes*, *20*(17), 3697–3708. https://doi.org/10.1002/hyp.6383

Stephens, G. L., Li, J., Wild, M., Clayson, C. A., Loeb, N., Kato, S., et al. (2012). An update on Earth's energy balance in light of the latest global observations. *Nature Geoscience*, *5*(10), 691–696. https://doi.org/10.1038/ngeo1580

Vargas Zeppetello, L. R., Donohoe, A., & Battisti, D. S. (2019). Does surface temperature respond to or determine downwelling longwave radiation? *Geophysical Research Letters*, *46*(5), 2781–2789. https://doi.org/10.1029/2019GL082220

Wan, Z., Hook, S., & Hulley, G. (2021a). MODIS/Terra land surface temperature/emissivity daily L3 global 1km SIN grid V061 [Dataset]. NASA EOSDIS Land Processes DAAC. https://doi.org/10.5067/MODIS/MOD11A1.061

Wan, Z., Hook, S., & Hulley, G. (2021b). MODIS/Terra land surface temperature/emissivity 8-day L3 global 1km SIN grid V061 [Dataset]. NASA EOSDIS Land Processes DAAC. https://doi.org/10.5067/MODIS/MOD11B2.061

Wan, Z., Hook, S., & Hulley, G. (2021c). MODIS/Terra land surface temperature/emissivity monthly L3 global 0.05Deg CMG V061 [Dataset]. NASA EOSDIS Land Processes DAAC. https://doi.org/10.5067/MODIS/MOD11C3.061

Webster, C., Rutter, N., & Jonas, T. (2017). Improving representation of canopy temperatures for modeling subcanopy incoming longwave radiation to the snow surface. *Journal of Geophysical Research: Atmospheres*, *122*(17), 9154–9172. https://doi.org/10.1002/2017JD026581

Weng, D. M., Chen, W. L., Shen, J. C., & Gao, J. B. (1981). *Microclimateand agricultural microclimate* (Chinese) (pp. 5–11). Agriculture Press.

Whiteman, C. D., & Hoch, S. W. (2010). Topographic effects on the surface radiation balance in and around Arizona's Meteor Crater. *Journal of Applied Meteorology and Climatology*, *49*(6), 1114–1128. https://doi.org/10.1175/2010jamc2353.1

Wild, M. (2020). The global energy balance as represented in CMIP6 climate models. *Climate Dynamics*, *55*(3), 553–577. https://doi.org/10.1007/s00382-020-05282-7

Wild, M., Ohmura, A., Gilgen, H., & Roeckner, E. (1995). Regional climate simulation with a high resolution GCM: Surface radiative fluxes. *Climate Dynamics*, *11*(8), 469–486. https://doi.org/10.1007/BF00207196

Wu, G. X., He, B., Duan, A. M., Liu, Y. M., & Yu, W. (2017). Formation and variation of the atmospheric heat source over the Tibetan Plateau and its climate effects. *Advances in Atmospheric Sciences*, *34*(10), 1169–1184. https://doi.org/10.1007/s00376-017-7014-5

Wu, Y., Wang, N., Li, Z., Chen, A., Guo, Z., & Qie, Y. (2019). The effect of thermal radiation from surrounding terrain on glacier surface temperatures retrieved from remote sensing data: A case study from Qiyi Glacier, China. *Remote Sensing of Environment*, *231*, 111267. https://doi.org/10.1016/j.rse.2019.111267

Xu, J., Zhang, X., Feng, C., Yang, S., Guan, S., Jia, K., et al. (2021). Evaluation of surface upward longwave radiation in the CMIP6 models with ground and satellite observations. *Remote Sensing*, *13*(21), 4464. https://doi.org/10.3390/rs13214464

Xu, J., Zhang, X., Zhang, W., Hou, N., Feng, C., Yang, S., et al. (2022). Assessment of surface downward longwave radiation in CMIP6 with comparison to observations and CMIP5. *Atmospheric Research*, *270*, 106056. https://doi.org/10.1016/j.atmosres.2022.106056

Yan, G., Jiao, Z. H., Wang, T., & Mu, X. (2020). Modeling surface longwave radiation over high-relief terrain. *Remote Sensing of Environment*, *237*, 111556. https://doi.org/10.1016/j.rse.2019.111556

Yan, G., Wang, T., Jiao, Z., Mu, X., Zhao, J., & Chen, L. (2016). Topographic radiation modeling and spatial scaling of clear-sky land surface longwave radiation over rugged terrain. *Remote Sensing of Environment*, *172*, 15–27. https://doi.org/10.1016/j.rse.2015.10.026

Yang, H., Shen, X., Yao, J., & Wen, Q. (2020). Portraying the impact of the Tibetan plateau on global climate. *Journal of Climate*, *33*(9), 3565–3583. https://doi.org/10.1175/jcli-d-18-0734.1

Yu, B., & Zhang, X. (2015). A physical analysis of the severe 2013/2014 cold winter in North America. *Journal of Geophysical Research: Atmospheres*, *120*(19), 10149–110165. https://doi.org/10.1002/2015JD023116

Zeng, Z., Piao, S., Li, L. Z., Zhou, L., Ciais, P., Wang, T., et al. (2017). Climate mitigation from vegetation biophysical feedbacks during the past three decades. *Nature Climate Change*, *7*(6), 432–436. https://doi.org/10.1038/nclimate3299

Zhang, H., Jing, X., & Li, J. (2014). Application and evaluation of a new radiation code under McICA scheme in BCC_AGCM2.0.1. *Geoscientific Model Development*, *7*(3), 737–754. https://doi.org/10.5194/gmd-7-737-2014

Zhang, T., Zhou, Y., Zhao, K., Zhu, Z., Chen, G., Hu, J., & Wang, L. (2022). A global dataset of daily maximum and minimum near-surface air temperature at 1 km resolution over land (2003–2020) [Dataset]. Earth System Science Data, *14*(12), 5637–5649. https://doi.org/10.5194/essd-14-5637-2022

Zhang, T., Zhou, Y., Zhu, Z., Li, X., & Asrar, G. R. (2022). A global seamless 1 km resolution daily land surface temperature dataset (2003–2020) [Dataset]. Earth System Science Data, *14*(2), 651–664. https://doi.org/10.5194/essd-14-651-2022

Zhang, Y., Huang, A., & Zhu, X. (2006). Parameterization of the thermal impacts of sub-grid orography on numerical modeling of the surface energy budget over East Asia. *Theoretical and Applied Climatology*, *86*(1–4), 201–214. https://doi.org/10.1007/s00704-005-0209-1

Zhang, Z., Zhou, X., & Li, W. (2002). Preliminary numerical study of topographic effects of the Tibetan Plateau on surface direct radiation. *Acta Meteorologica Sinica*, *16*(1), 51–61.

Zheng, W., Wei, H., Wang, Z., Zeng, X., Meng, J., Ek, M., et al. (2012). Improvement of daytime land surface skin temperature over arid regions in the NCEP GFS model and its impact on satellite data assimilation. *Journal of Geophysical Research*, *117*(D6), D06117. https://doi.org/10.1029/2011JD015901

Zhou, Q., & Liu, X. (2004). Analysis of errors of derived slope and aspect related to DEM data properties. *Computers & Geosciences*, *30*(4), 369–378. https://doi.org/10.1016/j.cageo.2003.07.005